

Tunable Intraband and Interband Polarizability in three-dimensional nodal line semimetals

Vivek Pandey,^{1,*} Snehasish Nandy,^{2,†} and Pankaj Bhalla^{1,3,‡}

¹Department of Physics, School of Engineering and Sciences, SRM University AP, Amaravati, 522240, India

²Department of Physics, National Institute of Technology, Silchar, Assam, 788010, India

³Centre for Computational and Integrative Sciences, SRM University AP, Amaravati, 522240, India

(Dated: July 8, 2025)

Polarizability plays an essential role in characterizing the key phenomena, such as the screening effects, collective excitations, and dielectric functions present in the system. In this study, we investigate the intraband and interband polarizability within the random phase approximation for the three-dimensional nodal line semimetals, specifically for Ca_3P_2 and ZrSiS . We find both intraband and interband contributions show tunable behavior with the chemical potential, which adds a resonance signature in the behavior of the polarizability. Further, in the long wavelength limit, the results reveal the quadratic dependence on the wave vector by the non-resonant intraband and interband parts of the polarizability. On the other hand, the resonant interband part gives a cubic dependence on the wave vector. In addition, the total polarizability is dominated by the intraband part in the low frequency regime, while in the mid and high frequency regimes, the interband part takes the lead. This study opens avenues for further theoretical and experimental exploration of frequency dependent dielectric properties, paving the way for potential applications in tunable plasmonic devices.

I. INTRODUCTION

The polarizability or density-density response function measures the response of a system to a perturbing scalar electric potential $\phi(\mathbf{q}, \omega)$ with wave vector \mathbf{q} and frequency ω and is defined within linear response theory as follows [1]:

$$\delta n(\mathbf{q}, \omega) = P(\mathbf{q}, \omega)\phi(\mathbf{q}, \omega). \quad (1)$$

Here, $\delta n(\mathbf{q}, \omega)$ represents the induced charge density due to the applied potential and $P(\mathbf{q}, \omega)$ refers to the polarizability. In the static case ($\omega = 0$), $P(\mathbf{q}, \omega)$ shows the screening of the impurity or Coulomb potential, while for the dynamic case ($\omega \neq 0$), it exhibits various phenomena such as plasmon excitations, optical absorption, etc. Moreover, polarizability serves as a central tool to probe electronic properties and examine the behavior of topological materials [1].

Topological materials are categorized into topological insulators and topological semimetals. The topological semimetals can be further classified into Dirac [2–8], Weyl [2, 9–17], and nodal line semimetals [18–30], based on the type of band touching between conduction and valence bands, which effects the response of the system. In topological insulators, the response is mainly contributed by the surface states, as the bulk states are gapped [31–35]. Upon doping, polarizability arising due to surface states shows linear dependence with the chemical potential μ and scales as q^2/ω with the wave vector and frequency at the low temperature and long

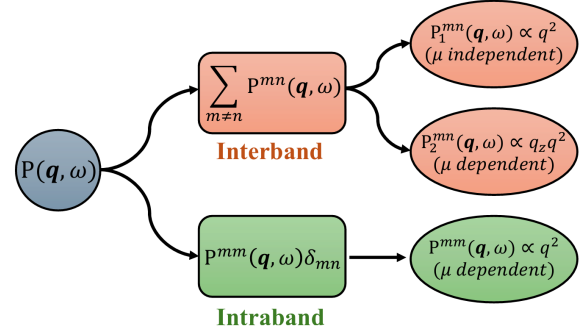


FIG. 1. The schematic shows the different components of polarizability $P(\mathbf{q}, \omega)$, which consist of two main contributions: the interband part, $\sum_{m \neq n} P^{mn}(\mathbf{q}, \omega)$, and the intraband part $P^{mm}(\mathbf{q}, \omega)\delta_{mn}$. Here, the wave vector is defined as $q = \sqrt{q_\rho^2 + q_z^2}$, with $q_\rho = \sqrt{q_x^2 + q_y^2}$. Further, the interband polarizability comprises of two parts, one is the μ independent and the other is the μ dependent part, which shows q^2 and $q_z q^2$ dependence, respectively. In contrast, the intraband part arises solely from μ dependent part.

wavelength limit, analogous to the two dimensional (2D) Dirac system [36, 37]. In the case of graphene, it is shown that the intrinsic contribution of static screening for long wavelength and temperature $T \rightarrow 0$ stems from the interband transitions and can be effectively absorbed in a background dielectric constant [36]. However, in 3D Dirac semimetals, where bands cross each other at a Dirac point, the polarizability at low temperature and long wavelength regime exhibits μ^2 and q^2/ω^2 behavior [37–40]. Weyl semimetals which require broken either space inversion (\mathcal{P}) or time-reversal (\mathcal{T}) symmetry or both depict similar polarizability behavior like Dirac semimetals. However, the presence of chiral anomaly can induce corrections to the polarizability [40]. In massive

* vivek.pandey@srmmap.edu.in

† snehasish@phy.nits.ac.in

‡ pankaj.b@srmmap.edu.in

Dirac systems, the dynamical polarization function has been analyzed and find the variation of screening potential as r^{-n} , where r represents the special decay rate and n refers to the dimensionality [39]. Additionally, the collective mode has been studied in various systems, including multi-Weyl semimetals [41] and a massless Dirac plasma [38], where it was observed that interband transitions and chirality lead to the depolarization shift in plasma frequencies [41].

On the contrary, the presence of the band crossing either in the form of a ring or line, which affects the density of the state [42], enriches the polarizability function of nodal line semimetals (NLSMs), which is sensitive to nodal ring radius, chemical potential, gap term, etc. In this context, Rahimpoor et al. and Yan et al. analyzed collective modes and dielectric function in 2D and 3D NLSMs [43, 44]. Herein, Ref. [44], the authors focus on the plasmon frequency derived from the intraband and interband parts of the polarizability within the long wavelength limit or the small \mathbf{q} limit. It is observed that the intraband component of polarizability depends on the chemical potential, whereas the interband component remains independent of it. However, the emergence of the resonant interband transitions can also make significant contributions to the interband part of the polarizability. Such transitions can be obtained by two ways: shifting the chemical potential to the edge of the conduction band and applying external energy equivalent to the gap between the conduction and valence bands. This particular aspect of the interband polarizability response has not been explored, motivating us to further in-depth exploration into the polarizability in 3D NLSMs.

In view of this, in this work, we consider the 3D NLSMs and calculates the intraband and interband parts of the polarizability and the dielectric function at low-temperature limits by employing the self-consistent field approximation, such as the random phase approximation (RPA), and using the low-energy two-band model for NLSMs. The present analysis focuses on the following key aspects: 1) The interband part of the polarizability contains a chemical potential-dependent term, which introduces a resonance feature in the interband response. 2) The interband polarizability shows dominance over the intraband component in the mid-frequency and high-frequency regimes. 3) The leading order interband polarizability comprises of both q^2 and $q_z q^2$ dependence terms, originating from the chemical potential independent and dependent parts, respectively. In particular, the $q_z q^2$ dependent term shows resonant behavior and under certain conditions, it can even exceed the q^2 dependent response. 4) Finally, we introduce the effect of the symmetry-breaking mass term, which leads to the non-trivial features in the polarizability. A schematic flow chart outlining the different contributions to the total polarizability is presented in Fig. 1.

The results further show that both the intraband

and the interband components of the polarizability are tunable with the chemical potential μ . In addition, the competition between the chemical potential and the mass term M can give rise to the metallic to insulating transition behavior. Finally, the analysis is tested for Ca_3P_2 and ZrSiS materials. Moreover, the presented theoretical approach is general and can be applied to other 3D systems.

II. POLARIZABILITY AND MODEL IN DIRAC NODAL LINE SEMIMETAL

For a non-interacting system, the polarizability is expressed as a density-density correlation function $\mathcal{P}(\mathbf{q}, t) = -i\theta(t)\langle[\hat{n}_{\mathbf{q}}(t), \hat{n}_{-\mathbf{q}}(0)]\rangle$, $\hat{n}_{\mathbf{q}}(t) = \sum_{n,\mathbf{k}} \hat{c}_{n,\mathbf{k}+\mathbf{q}}^\dagger(t)\hat{c}_{n,\mathbf{k}}(t)$ where $\hat{c}_{n,\mathbf{k}+\mathbf{q}}^\dagger(t)$ and $\hat{c}_{n,\mathbf{k}}(t)$ are the creation and annihilation operators associated with an electron having momentum $\mathbf{k} + \mathbf{q}$ and \mathbf{k} , $[\cdot, \cdot]$ denotes the commutation bracket and $\langle \dots \rangle$ is the expectation value in the ground state, respectively. Here we consider $\hbar = 1$, thus treating the wave vector as momentum and frequency as energy in the same way throughout the calculations. By employing the time-ordering to ensure causality and Wick's theorem to simplify the product of four creation and annihilation operators, the polarizability in the frequency domain can be written as $\mathcal{P}(\mathbf{q}, \omega) = \sum_{m,n} P^{mn}(\mathbf{q}, \omega)$ where

$$P^{mn}(\mathbf{q}, \omega) = \frac{1}{2v} \sum_{\mathbf{k}} \frac{f(\varepsilon_{\mathbf{k}+\mathbf{q}}^m) - f(\varepsilon_{\mathbf{k}}^n)}{\omega + \varepsilon_{\mathbf{k}+\mathbf{q}}^m - \varepsilon_{\mathbf{k}}^n + i\eta} |\langle m, \mathbf{k} + \mathbf{q} | n, \mathbf{k} \rangle|^2. \quad (2)$$

Here v corresponds to the volume of the system and is taken as unity for all calculations, $f(\varepsilon_{\mathbf{k}}^n)$ is the Fermi-Dirac distribution function that arises from the expectation value of the fermionic operators $\langle \hat{c}_{m,\mathbf{k}+\mathbf{q}}^\dagger \hat{c}_{n,\mathbf{k}} \rangle = \delta_{\mathbf{k}+\mathbf{q},\mathbf{k}} \delta_{mn} f(\varepsilon_{\mathbf{k}+\mathbf{q}}^m)$, where $\varepsilon_{\mathbf{k}}$ is the energy dispersion and m, n represent the band indices. Further, it is defined as $f(\varepsilon_{\mathbf{k}}^n) = [1 + e^{\beta(\varepsilon_{\mathbf{k}}^n - \mu)}]^{-1}$ with $\beta = 1/k_B T$ where k_B is the Boltzmann constant, T is the absolute temperature associated with an electron and μ refers to the chemical potential. Additionally, $|\langle m, \mathbf{k} + \mathbf{q} | n, \mathbf{k} \rangle|^2$ represents the matrix element between the electron's initial and final states, $|\langle m, \mathbf{k} + \mathbf{q} | n, \mathbf{k} \rangle|^2$ is the transition probability, which is defined as $|\langle m, \mathbf{k} + \mathbf{q} | n, \mathbf{k} \rangle|^2 = 1 + mn \cos 2\delta\theta_{\mathbf{k}\mathbf{q}}$, where $\delta\theta_{\mathbf{k}\mathbf{q}} = \theta_{\mathbf{k}+\mathbf{q}} - \theta_{\mathbf{k}}$ is the angle between \mathbf{k} and $\mathbf{k} + \mathbf{q}$ and lastly $\eta \rightarrow 0^+$ is a small positive infinitesimal number. Within the regime $q \rightarrow 0$ or long wavelength limit, a regime of our interest in the present study, several factors can be simplified in the following manner. (a) The difference between the distribution functions reduces as $f(\varepsilon_{\mathbf{k}+\mathbf{q}}^m) - f(\varepsilon_{\mathbf{k}}^n) = f(\varepsilon_{\mathbf{k}}^m) + \sum_{\gamma} q_{\gamma} \frac{\partial f(\varepsilon_{\mathbf{k}}^m)}{\partial \varepsilon_{\mathbf{k}}^m} - f(\varepsilon_{\mathbf{k}}^n)$, here $\gamma \equiv x, y, z$. (b) The energy difference associated with a different momentum $\varepsilon_{\mathbf{k}+\mathbf{q}}^m - \varepsilon_{\mathbf{k}}^n = \omega^{mn} + \sum_{\gamma} q_{\gamma} \frac{\partial \varepsilon_{\mathbf{k}}^m}{\partial \mathbf{k}_{\gamma}}$, here $\omega^{mn} = \varepsilon_{\mathbf{k}}^m - \varepsilon_{\mathbf{k}}^n$.

(c) The angular factor $\cos 2\delta\theta_{\mathbf{k}\mathbf{q}}^{mn} = \cos(\theta_{\mathbf{k}+\mathbf{q}}^m - \theta_{\mathbf{k}}^n) = \cos 2(\theta_{\mathbf{k}}^m - \theta_{\mathbf{k}}^n)(1 + \{2\sum_{\gamma} q_{\gamma}\partial_{\alpha}\theta_{\mathbf{k}}^m\}^2) + \dots$.

Within $q \rightarrow 0$ limit, the form of the polarizability given in Eq. (2) can be written as

$$P^{mn}(q \rightarrow 0, \omega) = \frac{1}{2} \sum_{\mathbf{k}} \frac{f^{mn} + \sum_{\gamma} q_{\gamma} \partial_{\gamma} f(\varepsilon_{\mathbf{k}}^m)}{\omega + \omega^{mn} + \sum_{\beta} q_{\beta} \partial_{\beta} \varepsilon_{\mathbf{k}}^m + i\eta} \times [1 + mn \cos 2\delta\theta_{\mathbf{k}}^{mn}(1 + \{2\sum_{\gamma} q_{\gamma} \partial_{\alpha} \theta_{\mathbf{k}}^m\}^2)]. \quad (3)$$

Here we define $f^{mn} = f(\varepsilon_{\mathbf{k}}^m) - f(\varepsilon_{\mathbf{k}}^n)$, $\partial_{\gamma} = \partial/\partial k_{\gamma}$ and $\delta\theta_{\mathbf{k}}^{mn} = \theta_{\mathbf{k}}^m - \theta_{\mathbf{k}}^n$.

To compute the polarizability in Dirac nodal line semimetals (DNLSMs), we consider an effective $\mathbf{k}\cdot\mathbf{p}$ two-band model Hamiltonian $\mathcal{H}(\mathbf{k}) = \varepsilon_0[(\tilde{\mathcal{K}} - 1)\sigma_x + \gamma\tilde{k}_z\sigma_y + \tilde{M}\sigma_z]$. The latter Hamiltonian has broken \mathcal{PT} symmetry [45–49]. The corresponding energy dispersion is

$$\tilde{\varepsilon}_{\mathbf{k}}^n = n\sqrt{(\tilde{\mathcal{K}} - 1)^2 + (\gamma\tilde{k}_z)^2 + \tilde{M}^2}. \quad (4)$$

Here, $\tilde{\varepsilon}_{\mathbf{k}}^n = \varepsilon_{\mathbf{k}}^n/\varepsilon_0$, where $\varepsilon_0 = k_0^2/(2m_e)$ is the energy associated with the nodal ring, k_0 is the nodal ring radius, m_e is the electronic mass and n is the band index associated with the conduction ($n = +$) band and valence ($n = -$) band. Further, $\tilde{\mathcal{K}} = \mathcal{K}/k_0$, here $\mathcal{K} = \sqrt{k_x^2 + k_y^2}$, the magnitude of the planar wave vector in $k_x - k_y$ plane, $\tilde{k}_z = k_z/k_0$ and $\gamma = 2m_e v_z/k_0$, where v_z is the component of Fermi velocity along z -direction, σ_i ($i \equiv x, y, z$) refers to the Pauli matrices in the pseudo spin basis. The $\tilde{M} = M/\varepsilon_0$, having M as the mass (gap) term that emerges experimentally from the application of an external magnetic field, pressure, stress, inversion-breaking uniaxial strain, etc., and is the source of the broken \mathcal{PT} symmetry of the system [46, 47, 50–54]. At $\tilde{M} = 0$, the nodal ring preserves all symmetry, such as \mathcal{P} , \mathcal{T} and \mathcal{PT} . In addition, the eigenvector is $|u_{\mathbf{k}}^n\rangle = \{\zeta_{\mathbf{k}}^- e^{-i\theta_{\mathbf{k}}}, \zeta_{\mathbf{k}}^+\}^T$, where $\zeta_{\mathbf{k}}^{\pm} = \pm \frac{1}{\sqrt{2}}[1 \pm \tilde{M}/\tilde{\varepsilon}_{\mathbf{k}}^n]^{1/2}$ and $\theta_{\mathbf{k}} = \tan^{-1}[\gamma\tilde{k}_z/(\tilde{\mathcal{K}} - 1)]$ the angle between the $\tilde{\mathcal{K}}$ plane and the \tilde{k}_z direction.

In the following subsections, we compute polarizability due to interband and intraband effects for the modeled Dirac nodal line semimetal and realistic material Ca_3P_2 and ZrSiS .

A. Interband Polarizability

Following Eq. (3), the interband part ($m \neq n$) of the polarizability P^{mn} within the low q limit for two band

model $m = +$ and $n = -$ can be expressed as

$$P^{+-}(\mathbf{q} \rightarrow 0, \omega) = \frac{1}{2} \sum_{\mathbf{k}} [1 - \cos 2\delta\theta_{\mathbf{k}\mathbf{q}}^{+-}] \times \frac{-1 + \Theta(\mu - \varepsilon_{\mathbf{k}}^+) + \sum_{\beta} q_{\beta} \frac{\partial \varepsilon_{\mathbf{k}}^+}{\partial k_{\beta}} \delta(\mu - \varepsilon_{\mathbf{k}}^+)}{\omega + 2\varepsilon_{\mathbf{k}} + i\eta}. \quad (5)$$

Note that here, we use the Fermi Dirac distribution function within the low temperature regime as $f(\varepsilon_{\mathbf{k}}^+) = \Theta(\mu - \varepsilon_{\mathbf{k}}^+)$, $f(\varepsilon_{\mathbf{k}}^-) = 1$, $\partial f(\varepsilon_{\mathbf{k}}^+)/\partial \varepsilon_{\mathbf{k}} = -\delta(\mu - \varepsilon_{\mathbf{k}}^+)$ and $\omega + \omega^{+-} + \sum_{\beta} q_{\beta} \partial_{\beta} \varepsilon_{\mathbf{k}}^+ + i\eta \approx \omega + 2\varepsilon_{\mathbf{k}} + i\eta$ with $\varepsilon_{\mathbf{k}}^+ = -\varepsilon_{\mathbf{k}}^-$. Here, two limits arise depending on the competition between the chemical potential and dispersion. In the first case $\mu < \varepsilon_{\mathbf{k}}$, $\Theta(\mu - \varepsilon_{\mathbf{k}}) = 1$, the only contribution arises from the term containing the delta function. In the second case $\mu > \varepsilon_{\mathbf{k}}$, the Heaviside theta function becomes $(\mu - \varepsilon_{\mathbf{k}}) = 0$. Clearly, the first two terms in Eq.(5) which we later together refer as P_1^{+-} give their variation independent of the chemical potential and it is shown for the considered system by the dashed lines in Fig. 2(a). The term associated with the shift in the distribution function or the delta function is referred to as P_2^{+-} and given below for considered system.

$$P_2^{+-} = \int_0^{\infty} \frac{\tilde{\mathcal{K}} d\tilde{\mathcal{K}} \tilde{q}_z [\gamma\tilde{q}_{\rho} \tilde{k}_{z0} - \gamma(\tilde{\mathcal{K}} - 1)\tilde{q}_z]^2}{4\pi^2 (\tilde{\omega} + 2\tilde{\mu} + i\eta)(\tilde{\mu}^2 - \tilde{M}^2)^2} \Theta(\tilde{k}_{z0}^2). \quad (6)$$

To obtain the above equation, we use the cylindrical coordinate system having $\tilde{q}_{\rho} = \sqrt{\tilde{q}_x^2 + \tilde{q}_y^2}$ and the angle term in the long-wavelength limit which reduces as $(1 - \cos 2\delta\theta_{\mathbf{k}\mathbf{q}}^{+-}) = \frac{2}{\tilde{\varepsilon}_{\mathbf{k}}^2 - \tilde{M}^2} \times (\gamma\tilde{k}_z \tilde{q}_{\rho} - \gamma\tilde{q}_z(\tilde{\mathcal{K}} - 1))$ and perform the integration over \tilde{k}_z using the property of the delta function. Here we define $\tilde{k}_{z0} = \sqrt{\tilde{\mu}^2 - (\tilde{\mathcal{K}} - 1)^2 - \tilde{M}^2}$, and insert a function $\Theta(\tilde{k}_{z0}^2)$ to ensure the existence of real solutions for \tilde{k}_z . From the latter function, a condition emerges $|\tilde{\mu}| > \sqrt{1 + \tilde{M}^2}$ which implies either $\tilde{\mu} < \sqrt{1 + \tilde{M}^2}$ or $\tilde{\mu} > \sqrt{1 + \tilde{M}^2}$. It is interesting to observe that P_2^{+-} part of the interband polarizability at $\tilde{q}_z \rightarrow 0$ vanishes. Furthermore, it yields resonances as the chemical potential touches the bottom of the conduction band. Here we can have two limiting cases as discussed below

Case-I: $\tilde{\mu} < \sqrt{1 + \tilde{M}^2}$, the integration limits for $\tilde{\mathcal{K}}$ lies between $-\tilde{\mu}$ to $\tilde{\mu}$. This yields

$$P_2^{+-} = \frac{\tilde{q}_z}{24\pi^2 (\tilde{\omega} + 2\tilde{\mu} + i\eta)(\tilde{\mu}^2 - \tilde{M}^2)^2} \times \left[\tilde{q}_{\rho}^2 \mathcal{B}_1(\tilde{M}, \tilde{\mu}) + \gamma\tilde{q}_z (\tilde{q}_{\rho} \mathcal{B}_2(\tilde{M}, \tilde{\mu}) + \gamma\tilde{q}_z \mathcal{B}_3(\tilde{M}, \tilde{\mu})) \right]. \quad (7)$$

Here, the term $\mathcal{B}_1(\tilde{M}, \tilde{\mu}) = 4\tilde{\mu}(2\tilde{\mu}^2 - 3\tilde{M}^2)$, $\mathcal{B}_2(\tilde{M}, \tilde{\mu}) = 3[\tilde{M}\tilde{\mu}(\tilde{M}^2 + \tilde{\mu}^2) - (\tilde{M}^2 - \tilde{\mu}^2)^2 \tan^{-1}(\frac{\tilde{\mu}}{\tilde{M}})]$ and $\mathcal{B}_3(\tilde{M}, \tilde{\mu}) = 4\tilde{\mu}^3$. Clearly, with the chemical potential $\tilde{\mu} \rightarrow 0$, the

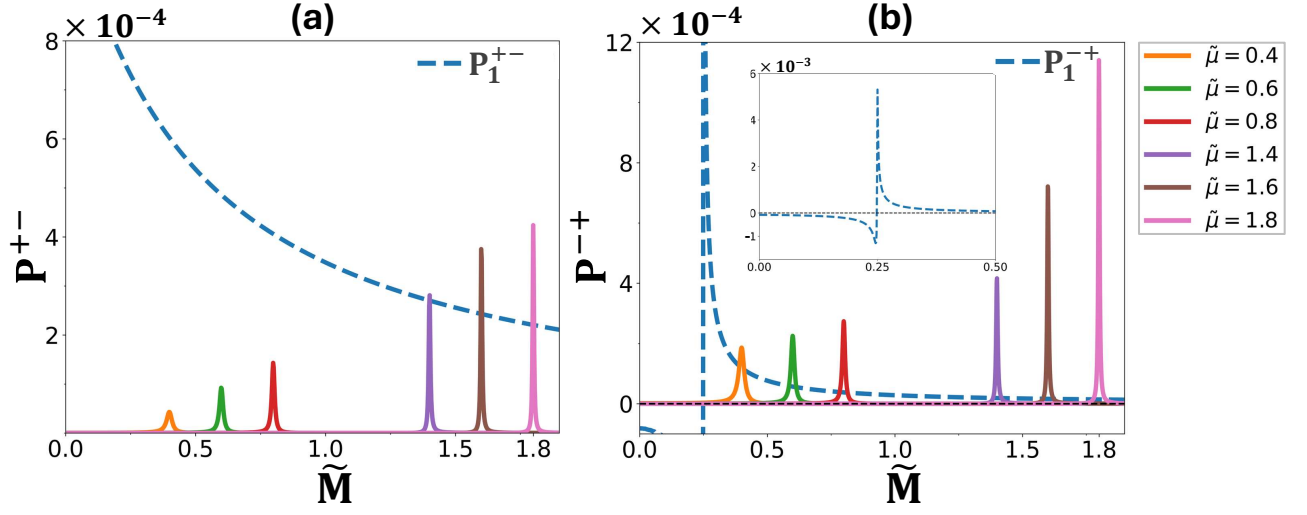


FIG. 2. Plot represents the interband part of the polarizability with mass values \tilde{M} for different chemical potential values $\tilde{\mu}$. (a) refers to the P^{+-} and (b) P^{-+} . Here, P_1^{+-} and P_1^{-+} refer to the $\tilde{\mu}$ independent part of interband polarizability of DNLSM. The inset in the figure (b) shows the complete variation of P_1^{-+} with \tilde{M} at a specific value of frequency. Here, we fix parameters like $\tilde{\omega} = 0.5$, $\tilde{q}_\rho = 0.01$, $\tilde{q}_z = 0.01$ and $\gamma = 2.8$.

P_2^{+-} vanishes. Further, as evident from the Eq. (7), it follows a different variation with chemical potential and mass term in comparison to the zero chemical potential case for the regime $\tilde{M} < 1$, $\tilde{\mu} < 1$. Specifically, the P_2^{+-} exhibits $\tilde{\mu}^{-1}$ when the Fermi level lies within the conduction band ($\tilde{\mu} > \tilde{M}$).

Case-II: $\tilde{\mu} > \sqrt{1 + \tilde{M}^2}$, the integration limits for $\tilde{\mathcal{K}}$ go from $-\sqrt{1 + \tilde{M}^2}$ to $\tilde{\mu}$ and the solution turns out to be quite complicated. Thus, it is better to express it in the following form

$$P_2^{+-} = \frac{\tilde{q}_z}{48\pi^2(\tilde{\omega} + 2\tilde{\mu} + i\eta)(\tilde{\mu}^2 - \tilde{M}^2)^2} \times \left[\tilde{q}_\rho^2 \mathcal{C}_1(\tilde{M}, \tilde{\mu}) + \gamma \tilde{q}_z \left(\tilde{q}_\rho \mathcal{C}_2(\tilde{M}, \tilde{\mu}) + \gamma \tilde{q}_z \mathcal{C}_3(\tilde{M}, \tilde{\mu}) \right) \right]. \quad (8)$$

The explicit forms of $\mathcal{C}_1(\tilde{M}, \tilde{\mu})$, $\mathcal{C}_2(\tilde{M}, \tilde{\mu})$ and $\mathcal{C}_3(\tilde{M}, \tilde{\mu})$ are quite large, and detailed expressions of these terms are provided in Appendix C. For the chemical potential larger than the gap value and keeping the gap value smaller than unity, here P_2^{+-} shows a dependence on $\tilde{\mu}^{-1}$.

On similar grounds, the second part of the interband polarizability P^{-+} yields an expression analogous to P^{+-} , with a slight change in the factor $\omega - 2\varepsilon_{\mathbf{k}} + i\eta$ which is present in the denominator. This factor gives the resonance at frequency equals to the gap between bands i.e., $\tilde{\omega} = 2\tilde{M}$. However, the other features remain qualitatively the same.

In Fig. 2(a), we present the interband part of the polarizability P^{+-} for DNLSM having two parts: P_1^{+-} the chemical potential independent part shown by the dashed line and P_2^{+-} the chemical potential dependent part displayed by the solid line. The $\tilde{\mu}$ independent part originates from transitions far away from the Fermi level

and explains the kind of background interband response of the nodal line system. This contribution decreases with an increase in the \tilde{M} band gap value, scales as \tilde{M}^{-1} and with frequency scales as $\tilde{\omega}^{-2}$. Therefore, this contribution is significant at small band gap values and low frequencies. In addition, the $\tilde{\mu}$ dependent part shows resonant interband transitions when the chemical potential approaches the gap value $\tilde{\mu} = \tilde{M}$, and the strength of the peaks increases with increasing $\tilde{\mu}$. However, for the chemical potential deeper in the conduction band ($\tilde{\mu} > \tilde{M}$), most of the interband transitions are Pauli blocked, thus reducing the response.

On the other hand, Fig. 2(b) illustrates the P^{-+} part of the interband polarizability in a DNLSM. Here, the $\tilde{\mu}$ independent part of the interband polarizability exhibits resonance features followed by prominent transition peaks at $\tilde{M} = \tilde{\omega}/2$, indicative of Kramers-Kronig-type dispersive features. This is a universal feature of interband polarizability at the band edge. The $\tilde{\mu}$ dependent component of the interband polarizability follows a similar behavior as observed in Fig. 2(a), with slight differences arising due to the weighted factors. At a large value of \tilde{M} , the band gap becomes significantly larger, making the fixed photon energy $\tilde{\omega}$, insufficient to excite the electrons across the band gap. As a result, the interband transition becomes blocked, and the polarizability gradually diminishes.

B. Intraband Polarizability

The origin of the intraband polarizability comes from the single-band dynamics. For the two-band model system, the intraband polarizability comprises of two components: P^{++} comes purely from the conduction

band, and P^{--} from the valence band. First, the P^{++} intraband part of the polarizability Eq. (3) by setting $m = n = +$ becomes

$$P^{++}(q \rightarrow 0, \tilde{\omega}) = - \sum_{\mathbf{k}} \sum_{\gamma, \beta} \frac{\tilde{q}_\beta \tilde{q}_\gamma}{\tilde{\omega}^2} \frac{\partial \tilde{\varepsilon}_{\mathbf{k}}^+}{\partial \tilde{k}_\beta} \frac{\partial \tilde{\varepsilon}_{\mathbf{k}}^+}{\partial \tilde{k}_\gamma} \frac{\partial f(\tilde{\varepsilon}_{\mathbf{k}}^+)}{\partial \tilde{\varepsilon}_{\mathbf{k}}^+}. \quad (9)$$

Here, we expand the factor $[\tilde{\omega} + \frac{\partial \tilde{\varepsilon}_{\mathbf{k}}}{\partial k_\gamma} \tilde{q}_\gamma]^{-1} = 1/\tilde{\omega}(1 - \frac{\partial \tilde{\varepsilon}_{\mathbf{k}}}{\partial k_\gamma} \frac{\tilde{q}_\gamma}{\tilde{\omega}})$ and keep the non-zero leading order term in $\tilde{\mathbf{q}}$ for DNLSM. Clearly, the intraband part of the polarizability shows a quadratic dependence on $|\tilde{\mathbf{q}}|$ and inverse square law with $\tilde{\omega}$. Further on approximating the energy derivative of the Fermi Dirac distribution function $-\delta(\tilde{\mu} - \tilde{\varepsilon}_{\mathbf{k}})$ at the low-temperature limit and performing summations over $\gamma, \beta = \{x, y, z\}$, the intraband part of the polarizability for the modeled DNLSM simplifies to

$$P^{++} = \frac{1}{\tilde{\omega}^2} \int_0^\infty \frac{d\tilde{K}\tilde{K}}{4\pi^2\gamma^2} \frac{1}{\tilde{\mu}\tilde{k}_{z0}} [(\tilde{K} - 1)^2 \tilde{q}_\rho^2 + \gamma^2 \tilde{k}_{z0}^2 \tilde{q}_z^2] \Theta(\tilde{k}_{z0}^2). \quad (10)$$

Here we use the properties of the delta function to perform the integration over \tilde{k}_z and introduce $\Theta(\tilde{k}_{z0}^2)$ which guarantees the existence of the real solutions for \tilde{k}_z . However, analogous to the interband part of the polarizability, here we have two limiting cases, with $\tilde{\mu} < \sqrt{1 + \tilde{M}^2}$ or $\tilde{\mu} > \sqrt{1 + \tilde{M}^2}$.

Case-I: $\tilde{\mu} < \sqrt{1 + \tilde{M}^2}$, P^{++} becomes

$$P^{++} = \frac{1}{4\pi^2\gamma^2\tilde{\mu}\tilde{\omega}^2} [\mathcal{F}(\tilde{M}, \tilde{\mu})(\tilde{q}_\rho^2 + \gamma^2\tilde{q}_z^2) + 2\tilde{M}\tilde{\mu}\gamma^2\tilde{q}_z^2], \quad (11)$$

where $\mathcal{F}(\tilde{M}, \tilde{\mu}) = -[(\tilde{M}^2 - \tilde{\mu}^2) \tan^{-1}(\tilde{\mu}/\tilde{M}) + \tilde{M}\tilde{\mu}]$. To understand the behavior of the intraband polarizability given in Eq. (11), we can categorize the analysis into two different regimes depending on the variation of \tilde{M} and $\tilde{\mu}$. First, we consider the regime $\tilde{M} < 1$, $\tilde{\mu} < 1$. Here, the intraband polarizability follows $\tilde{\mu} \tan^{-1}(\tilde{\mu}/\tilde{M})$ behavior on taking the chemical potential larger than the gap value. While for $\tilde{\mu} < \tilde{M}$, it yields linear dependence in \tilde{M} . In the second regime, defined by $\tilde{M} > 1$, $\tilde{\mu} < \tilde{M}$, two scenarios arise $\tilde{\mu} < 1$ and $\tilde{\mu} > 1$, which exhibits a linear dependence on \tilde{M} .

Case-II: $\tilde{\mu} > \sqrt{1 + \tilde{M}^2}$, the interband polarizability P^{++} becomes,

$$P^{++} = \frac{1}{24\pi^2\gamma^2\tilde{\mu}\tilde{\omega}^2} \left[\mathcal{A}_1(\tilde{M}, \tilde{\mu}) \tilde{q}_\rho^2 + \mathcal{A}_2(\tilde{M}, \tilde{\mu}) \gamma^2 \tilde{q}_z^2 \right]. \quad (12)$$

Here, the explicit forms of $\mathcal{A}_1(\tilde{M}, \tilde{\mu})$, and $\mathcal{A}_2(\tilde{M}, \tilde{\mu})$ are quite cumbersome and are provided in the Appendix A. However, we discuss these factors within the limiting regime. In the regime $\tilde{M} < 1$, $\tilde{\mu} > 1$ which ensures the chemical potential is greater than the mass value, i.e., $\tilde{\mu} > \tilde{M}$, both factors $\mathcal{A}_1(\tilde{M}, \tilde{\mu})$ and

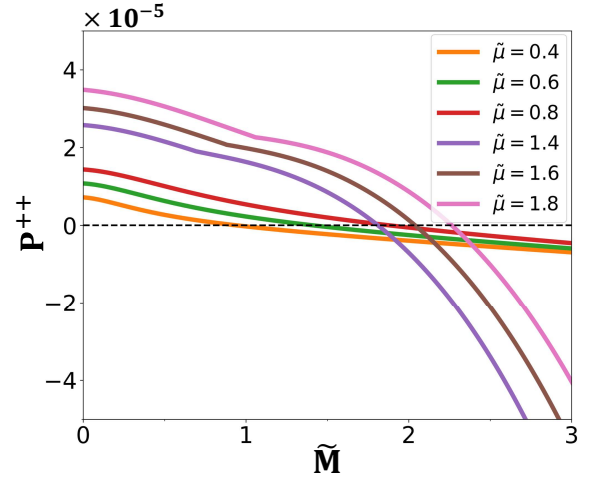


FIG. 3. Plot for the P^{++} component of the intraband part of the polarizability with mass values \tilde{M} for different values of $\tilde{\mu}$. Here, we fix $\tilde{\omega} = 0.5$, $\tilde{q}_\rho = 0.01$, $\tilde{q}_z = 0.01$ and $\gamma = 2.8$.

$\mathcal{A}_2(\tilde{M}, \tilde{\mu})$ show dependencies on $\tilde{\mu}^2 \tan^{-1}(\tilde{\mu}/\tilde{M})$ and $\tilde{\mu}^3$. Therefore, the intraband polarizability within this regime follows a pattern depending on the competition between $\tilde{\mu} \tan^{-1}(\tilde{\mu}/\tilde{M})$ and $\tilde{\mu}^2$.

In Fig. 3, we demonstrate the variation of the intraband part of the polarizability, P^{++} with the mass values \tilde{M} for different values of the chemical potential $\tilde{\mu}$. Here, we observe two different patterns depending on the chemical potential taken into account, as previously discussed in Eqs. (11) and (12). In the regime $\tilde{\mu} < 1$, the intraband polarizability yields finite value in the absence of the mass term i.e., at $\tilde{M} = 0$. This behavior arises due to the finite density of states around the protected nodal ring and indicates the metallic nature of the system. On turning the mass term on, $\tilde{M} \neq 0$, the intraband polarizability decreases, followed by a sign change and linear variation with \tilde{M} . The resulting behavior is controlled by the position of the chemical potential (Fermi level) within the conduction band and in the gaped region. Here the location of the phase change where the intraband polarizability vanishes occurs at \tilde{M} higher than $\tilde{\mu}$. This sign-flipping behavior indicates the transition from the metallic to the insulating region. Additionally, the magnitude of the intraband polarizability also increases with the chemical potential, while the qualitative behavior of the intraband polarizability remains unchanged. These results are consistent with the power law dependence discussed in Eq. (11).

In the regime $\tilde{\mu} > \sqrt{1 + \tilde{M}^2}$, there can be two possibilities: one when $\tilde{M} < 1$, $\tilde{\mu} > 1$, which ensures that the chemical potential is greater than the mass term $\tilde{\mu} > \tilde{M}$ (the Fermi surface is no longer a torus), as discussed in Eq. (12). Here, at $\tilde{M} = 0$ the intraband part of the polarizability remains non-zero polarizability due to the finite density of state at the Fermi energy

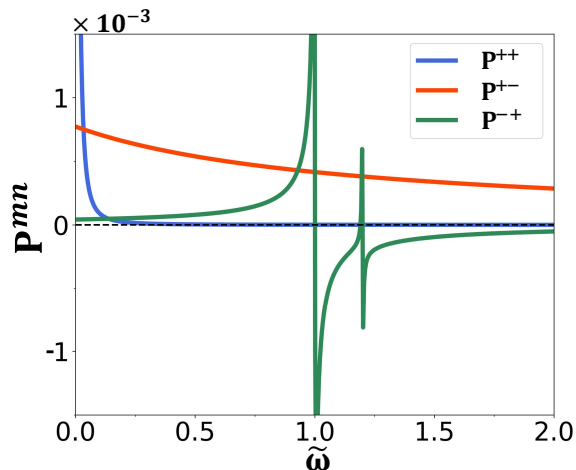


FIG. 4. depicts the comparison between the intraband and the interband components of the polarizability with the frequency $\tilde{\omega}$ at fixed $\tilde{\mu} = 0.6$, $\tilde{M} = 0.5$, $\tilde{q}_\rho = 0.01$, $\tilde{q}_z = 0.01$ and $\gamma = 2.8$.

(shows a metal-like screening). In addition, on moving towards higher mass value and from $\tilde{M} < 1$ to $\tilde{M} > 1$ regime the polarizability decreases, followed by a sign change in the polarizability. Beyond this point, the system follows a different power law due to the interplay of contributions associated with perpendicular and parallel $\tilde{\mathbf{q}}$ components. Moreover, an increase in the chemical potential $\tilde{\mu}$ enhances the overall magnitude of the response and shifts the location of both the sign change and dip to the higher \tilde{M} . Despite these shifts, the qualitative behavior of the system remains unchanged.

Furthermore, the other component of the intraband polarizability P^{--} yields zero results in the low-temperature limit due to the vanishing difference between the Fermi Dirac distribution functions. More details are provided in the Appendix B.

Fig. 4 presents a comparison plot between the intraband (P^{++}) and the interband (P^{+-} and P^{-+}) contributions to the polarizability of the DNLSM as a function of frequency $\tilde{\omega}$. We find the dominating nature of the intraband polarizability of the DNLSMs in a lower frequency regime. The resulting intraband feature shows the Drude-like nature and scales by $\tilde{\omega}^{-2}$. However, as the frequency increases into the intermediate- and high-frequency regimes, the interband contributions become increasingly significant and eventually dominate the overall polarizability of the DNLSM. In addition, a distinct transition peak emerges which originates from the interband component of the polarizability, and it signifies the optical absorption, a similar resonance peak at $\tilde{\omega} = 2\tilde{\mu}$ has been observed in Ref. [45].

III. DIELECTRIC FUNCTION

The dielectric function within the random phase approximation (RPA) is defined as

$$\epsilon^{RPA}(\tilde{\mathbf{q}}, \tilde{\omega}) = 1 - v(\tilde{\mathbf{q}})P^{mn}(\tilde{\mathbf{q}}, \tilde{\omega}). \quad (13)$$

Here, $P^{mn}(\tilde{\mathbf{q}}, \tilde{\omega}) = P^{mm}(\tilde{\mathbf{q}}, \tilde{\omega})\delta_{mn} + \sum_{m \neq n} P^{mn}(\tilde{\mathbf{q}}, \tilde{\omega})$, where $P^{mm}(\tilde{\mathbf{q}}, \tilde{\omega}) = \zeta(\tilde{\mathbf{q}})/\tilde{\omega}^2$, here $\zeta(\tilde{\mathbf{q}})$ is the frequency independent part arising from Eq. (10) and P^{mn} is the interband part of the polarizability. Furthermore the $v(\tilde{\mathbf{q}}) = 4\pi e^2/k_b k_0^2 \tilde{\mathbf{q}}^2$, is the Coulomb potential in momentum space, where k_b is the background dielectric constant and $\tilde{q} = \sqrt{\tilde{q}_\rho^2 + \tilde{q}_z^2}$. In the case of plasmon frequency,

$$0 = 1 - v(\tilde{\mathbf{q}})[P^{mm}(\tilde{\mathbf{q}}, \tilde{\omega}) + \sum_{m \neq n} P^{mn}(\tilde{\mathbf{q}}, \tilde{\omega})]. \quad (14)$$

It is important to note that the plasmon frequency is determined by the condition where the dielectric function becomes zero, i.e., $\epsilon^{RPA}(\tilde{\mathbf{q}}, \tilde{\omega}) = 0$. This condition is stable in the region where the intraband contribution has a dominant effect, specifically in $\tilde{\omega} < \tilde{\mu}$ region. Hence, in this limit, the interband contribution to the polarizability becomes frequency independent and the plasmon frequency is given by the expression,

$$\omega_p = \sqrt{\frac{v(\tilde{\mathbf{q}})\zeta(\tilde{\mathbf{q}})}{1 - v(\tilde{\mathbf{q}})\sum_{m \neq n} P^{mn}(\tilde{\mathbf{q}})}}. \quad (15)$$

Here, the polarizability comprises contributions associated with the \tilde{q}_ρ and \tilde{q}_z components of the wave vector. To understand the plasmon frequency variation for DNLSMs stemming from the \tilde{q}_ρ and \tilde{q}_z components of the wave vector, we add the analysis below.

In the case of \tilde{q}_ρ component ($\tilde{q}_z \rightarrow 0$), the plasmon frequency becomes

$$\omega_{p,\rho} = \sqrt{\frac{v(\tilde{q}_\rho)\zeta(\tilde{q}_\rho)}{1 - v(\tilde{q}_\rho)\sum_{m \neq n} P_1^{mn}(\tilde{q}_\rho)}}. \quad (16)$$

In this case, the contribution to the plasmon frequency comes from the intraband and the P_1^{+-} part of the interband polarizability, as the P_2^{+-} part is $\propto \tilde{q}_z$ (as shown in Eq (6)), thus vanishes in this limit. Furthermore, the Fermi energy dependence solely arises from the intraband component, whereas the P_1^{+-} component remains independent of the chemical potential.

In contrast, in the case of the plasmon frequency coming from the \tilde{q}_z component ($\tilde{q}_\rho \rightarrow 0$), we obtain

$$\omega_{p,z} = \sqrt{\frac{v(\tilde{q}_z)\zeta(\tilde{q}_z)}{1 - v(\tilde{q}_z)\sum_{m \neq n} P^{mn}(\tilde{q}_z)}}. \quad (17)$$

Here, the behavior of the plasmon frequency depends on both the variation of the intraband and interband parts of the polarizability in DNLSM, as discussed in the Sec. II B and Sec. II A.

The plasmon frequency, in the presence of both components of wave vector (i.e., \tilde{q}_ρ and \tilde{q}_z), shows a complex dependency on the wave vector. However, the leading order contribution with an individual component \tilde{q}_ρ and \tilde{q}_z to the polarizability reveals the wave vector independent and dependent behavior of the plasmon frequency, respectively.

IV. EXPERIMENTAL RELEVANCE AND NUMERICAL ESTIMATION

Experimentally, the dielectric function of materials can be determined using techniques such as optical spectroscopy in the low-momentum regime and electron energy loss spectroscopy in high momentum regime. Since polarizability is a more microscopic quantity and is not directly measurable, it is typically calculated from the dielectric function. First, the intraband and interband contributions to the polarizability and to dielectric function can be distinguished by modulating the applied oscillating field. Further, the separation of the resonant and non-resonant parts of the interband polarizability can be achieved by systematically tuning the parameters such as the chemical potential, frequency, and gap. These can be controlled using methods like electrostatic gating or doping (for chemical potential), optical excitation (for frequency), and strain engineering (for the gap). In particular, the peaks led by interband transitions for polarizability at $\tilde{\omega} = 2\tilde{M}$ and $\tilde{\mu} = \tilde{M}$ can be probed by modulating the external applied field and doping. Here, the position and strength of such features are sensitive to the band gap, making it an important parameter for the polarizability.

For the numerical estimation of the polarizability of Dirac nodal line semimetals, we consider Ca_3P_2 and ZrSiS as promising materials due to their nodal line structure and tunable transport and optical properties. For Ca_3P_2 , we have used the DFT fitted parameters, such as radius of the nodal ring $k_0 \approx 0.206\text{\AA}^{-1}$ and the energy associated with the nodal ring $\varepsilon_0 \approx 0.184$ eV and the parameter $\gamma \approx 2.80$ [23, 55]. At a frequency $\tilde{\omega} = 0.5$ (where $\tilde{\omega} = \omega/\varepsilon_0$), $\tilde{\mu} = 1.4$ and $\tilde{M} = 1.4$, the intraband polarizability is $P^{mm} = 1.05 \times 10^{-5} \text{ eV}^{-1} \text{ m}^{-3}$, while the interband part $P^{mn} = P_1^{mn} + P_2^{mn} \approx 8.38 \times 10^{-4} \text{ eV}^{-1} \text{ m}^{-3}$. Here, the $\tilde{\mu}$ independent and dependent parts, P_1^{mn} and P_2^{mn} respectively, relate as $P_2^{mn} \approx 5P_1^{mn}$. In addition, we find $P^{mn} \approx 80P^{mm}$. In the case of

ZrSiS , we consider $k_0 \approx 4.3\text{\AA}^{-1}$, $\varepsilon_0 \approx 70$ eV and $\gamma \approx 0.20$ [56]. Here, at frequency $\tilde{\omega} = 0.5$, $\tilde{\mu} = 1.4$ and $\tilde{M} = 1.4$, the intraband part of polarizability yields $P^{mm} = 2.9 \times 10^{-4} \text{ eV}^{-1} \text{ m}^{-3}$, while the interband part gives $P^{mn} = 1.77 \times 10^{-4} \text{ eV}^{-1} \text{ m}^{-3}$. Here the $P_2^{mn} \approx 8P_1^{mn}$ and the $P^{mm} \approx 1.5P^{mn}$. It shows that, in the case of ZrSiS , the intraband and interband contributions are comparable to each other. However, the interband to intraband ratio is not large as compared to Ca_3P_2 due to large nodal ring radius. These estimates infer that such variations can be significantly observed as well with materials having a nodal ring radius smaller than that of ZrSiS .

V. SUMMARY

In summary, we have investigated the polarizability of a three-dimensional Dirac nodal line semimetal in the long wavelength and low temperature regime. We have shown that the intraband polarizability exhibits a \tilde{q}^2 dependence and comes solely from the chemical potential dependence part. However, contributions to the interband polarizability arise from the two distinct contributions: a resonant ($\tilde{\mu}$ dependent) component and a non-resonant ($\tilde{\mu}$ independent) component and shows \tilde{q}^2 and $\tilde{q}_z\tilde{q}^2$ dependence, respectively. We further showed that while the resonant part of interband polarizability can be tunable via chemical potential, the nonresonant term is primarily tunable through the frequency. Additionally, the mass (gap) term modulates both contributions, influencing the overall interband response. At low frequencies, the total polarizability is dominated by the intraband response, whereas at intermediate and high frequencies, the interband response gives a dominant contribution. In this regime, the contribution of the chemical potential dependent interband response plays a crucial role and cannot be neglected. Furthermore, the sign flipping of intraband polarizability can be beneficial to track the metal to insulator transition. Finally, one can extend the present framework to investigate the effect of tilt [57], which breaks the inversion symmetry and can be further generalized for the analysis of other 3D systems [30, 58].

VI. ACKNOWLEDGMENT

This work is financially supported by the Science and Engineering Research Board-State University Research Excellence under project number SUR/2022/000289.

Appendix A: Explicit forms of functions used in the Eq. (12)

The expression for the intraband polarizability, as presented in Eq. (12)

$$P^{++} = \frac{1}{24\pi^2\gamma^2\tilde{\mu}\tilde{\omega}^2} \left[\mathcal{A}_1(\tilde{M}, \tilde{\mu}) \tilde{q}_\rho^2 + \mathcal{A}_2(\tilde{M}, \tilde{\mu}) \gamma^2 \tilde{q}_z^2 \right], \quad (\text{A1})$$

where the function $\mathcal{A}_i(\tilde{M}, \tilde{\mu})$ ($i = 1, 2$) is defined as:

$$\mathcal{A}_i(\tilde{M}, \tilde{\mu}) = \mathcal{G}(\tilde{M}, \tilde{\mu}) + \tilde{M} a_i(\tilde{M}, \tilde{\mu}) + \sqrt{|\tilde{\mu}^2 - 2\tilde{M}^2 - 1|} \Delta_i(\tilde{M}, \tilde{\mu}). \quad (\text{A2})$$

The auxiliary functions used in the above expression are given by:

$$\begin{aligned} \mathcal{G}(\tilde{M}, \tilde{\mu}) &= 3(\tilde{\mu}^2 - \tilde{M}^2) \left(\tan^{-1} \left[\frac{\tilde{\mu}}{\tilde{M}} \right] + \tan^{-1} \left[\frac{\sqrt{1 + \tilde{M}^2}}{\sqrt{|\tilde{\mu}^2 - 2\tilde{M}^2 - 1|}} \right] \right) \\ a_1(\tilde{M}, \tilde{\mu}) &= 4\tilde{M}^2 - 3\tilde{\mu}(2\tilde{\mu} + 1), & \Delta_1(\tilde{M}, \tilde{\mu}) &= 4\tilde{\mu}^2 - 2\tilde{M}^2 - 3\sqrt{1 + \tilde{M}^2} + 2 \\ a_2(\tilde{M}, \tilde{\mu}) &= 2\tilde{M}^2 + 3\tilde{\mu}, & \Delta_2(\tilde{M}, \tilde{\mu}) &= 2\tilde{\mu}^2 - 4\tilde{M}^2 + 3\sqrt{1 + \tilde{M}^2} - 2. \end{aligned}$$

Appendix B: Derivation of component of Intraband polarizability P^{--}

The general form of polarizability is

$$P^{--}(\mathbf{q}, \omega) = \frac{1}{2v} \sum_{\mathbf{k}} \frac{f(\varepsilon_{\mathbf{k}+\mathbf{q}}^-) - f(\varepsilon_{\mathbf{k}}^-)}{\omega + \varepsilon_{\mathbf{k}+\mathbf{q}}^- - \varepsilon_{\mathbf{k}}^- + i\eta} |\langle m, \mathbf{k} + \mathbf{q} | n, \mathbf{k} \rangle|^2. \quad (\text{B1})$$

In the low-temperature limit, the Fermi Dirac distribution function reduces to the Heaviside theta function, i.e., $f(\varepsilon_{\mathbf{k}}) = \Theta(\mu - \varepsilon_{\mathbf{k}})$, hence the above equation becomes,

$$P^{--}(\mathbf{q}, \omega) = \frac{1}{2v} \sum_{\mathbf{k}} \frac{\Theta(\mu + \varepsilon_{\mathbf{k}+\mathbf{q}}) - \Theta(\mu + \varepsilon_{\mathbf{k}})}{\omega - \varepsilon_{\mathbf{k}+\mathbf{q}} + \varepsilon_{\mathbf{k}} + i\eta} \times (1 + \cos 2\delta\theta_{\mathbf{k}\mathbf{q}}) \quad (\text{B2})$$

The Heaviside theta function is defined as $\Theta(x) = 0$ for $x < 0$ and $\Theta(x) = 1$ for $x > 0$. In the above expression, $\Theta(\mu + \varepsilon_{\mathbf{k}}) = 1$ when $\mu + \varepsilon_{\mathbf{k}} > 0$, which satisfies conditions $\varepsilon_{\mathbf{k}} > 0$ and $\mu > 0$. Under this condition, both $\Theta(\mu + \varepsilon_{\mathbf{k}+\mathbf{q}})$ and $\Theta(\mu + \varepsilon_{\mathbf{k}})$ become 1, and the term $\Theta(\mu + \varepsilon_{\mathbf{k}+\mathbf{q}}) - \Theta(\mu + \varepsilon_{\mathbf{k}}) = 1 - 1 = 0$. As a result, the P^{--} contribution to the intraband polarizability vanishes. In addition, when $\Theta(\mu + \varepsilon_{\mathbf{k}}) = 0$ for $\mu + \varepsilon_{\mathbf{k}} < 0$, the step function becomes zero, hence P^{--} zero.

Appendix C: Explicit forms of functions used in Eq. (8)

The expression for the P^{+-} part of interband polarizability, as presented in Eq. (8)

$$P_2^{+-} = \frac{\tilde{q}_z}{48\pi^2(\tilde{M}^2 - \tilde{\mu}^2)^2(2\tilde{\mu} + \tilde{\omega})} \left[\tilde{q}_\rho^2 \mathcal{C}_1(\tilde{M}, \tilde{\mu}) + \gamma \tilde{q}_z \left(\tilde{q}_\rho \mathcal{C}_2(\tilde{M}, \tilde{\mu}) + \gamma \tilde{q}_z \mathcal{C}_3(\tilde{M}, \tilde{\mu}) \right) \right]. \quad (\text{C1})$$

Here,

$$\begin{aligned} \mathcal{C}_1(\tilde{M}, \tilde{\mu}) &= 3 - 4S + \tilde{M}^2(12 - 16S - 12\tilde{\mu}(1 + \tilde{\mu})) + \tilde{\mu}^2(-6 + 12S + \tilde{\mu}(8 + 3\tilde{\mu})) + 9\tilde{M}^4 \\ \mathcal{C}_2(\tilde{M}, \tilde{\mu}) &= 2(4 - 3S)R - \tilde{M}^2(8\tilde{M} + 3\tilde{M}\tilde{\mu} - 16R + 9SR) + \tilde{\mu}^2(-3\tilde{M}\tilde{\mu} + (-8 + 3S)R) \\ &\quad - 3(\tilde{M}^2 - \tilde{\mu}^2)^2 \left(\tan^{-1} \left[\frac{\tilde{\mu}}{\tilde{M}} \right] + \tan^{-1} \left[\frac{S}{R} \right] \right) \\ \mathcal{C}_3(\tilde{M}, \tilde{\mu}) &= -3 + 4S + \tilde{M}^2(-6 + 4S) + \tilde{\mu}^3(4 + 3\tilde{\mu}) - 3\tilde{M}^4, \end{aligned} \quad (\text{C2})$$

where terms $S = \sqrt{1 + \tilde{M}^2}$, and $R = \sqrt{|\tilde{\mu}^2 - 2\tilde{M}^2 - 1|}$.

-
- [1] Gabriele Giuliani and Giovanni Vignale, *Quantum theory of the electron liquid* (Cambridge university press, 2008).
- [2] N. P. Armitage, E. J. Mele, and Ashvin Vishwanath, “Weyl and dirac semimetals in three-dimensional solids,” *Rev. Mod. Phys.* **90**, 015001 (2018).
- [3] S. M. Young, S. Zaheer, J. C. Y. Teo, C. L. Kane, E. J. Mele, and A. M. Rappe, “Dirac semimetal in three dimensions,” *Phys. Rev. Lett.* **108**, 140405 (2012).
- [4] ZK Liu, Jianzhong Jiang, Bo Zhou, ZJ Wang, Yi Zhang, HM Weng, Dharmalingam Prabhakaran, Sung Kwan Mo, Han Peng, Pavel Dudin, *et al.*, “A stable three-dimensional topological dirac semimetal Cd₃As₂,” *Nature materials* **13**, 677–681 (2014).
- [5] Sergey Borisenko, Quinn Gibson, Danil Evtushinsky, Volodymyr Zabolotnyy, Bernd Büchner, and Robert J. Cava, “Experimental realization of a three-dimensional dirac semimetal,” *Phys. Rev. Lett.* **113**, 027603 (2014).
- [6] Hemian Yi, Zhijun Wang, Chaoyu Chen, Youguo Shi, Ya Feng, Aiji Liang, Zhuojin Xie, Shaolong He, Junfeng He, Yingying Peng, *et al.*, “Evidence of topological surface state in three-dimensional dirac semimetal Cd₃As₂,” *Scientific Reports* **4**, 6106 (2014).
- [7] Zhijun Wang, Hongming Weng, Quansheng Wu, Xi Dai, and Zhong Fang, “Three-dimensional dirac semimetal and quantum transport in Cd₃As₂,” *Phys. Rev. B* **88**, 125427 (2013).
- [8] ZK Liu, Bo Zhou, Yong Zhang, ZJ Wang, HM Weng, Dharmalingam Prabhakaran, S-K Mo, ZX Shen, Zhong Fang, Xi Dai, *et al.*, “Discovery of a three-dimensional topological dirac semimetal, Na₃Bi,” *Science* **343**, 864–867 (2014).
- [9] Binghai Yan and Claudia Felser, “Topological materials: Weyl semimetals,” *Annual Review of Condensed Matter Physics* **8**, 337–354 (2017).
- [10] B. Q. Lv, H. M. Weng, B. B. Fu, X. P. Wang, H. Miao, J. Ma, P. Richard, X. C. Huang, L. X. Zhao, G. F. Chen, Z. Fang, X. Dai, T. Qian, and H. Ding, “Experimental discovery of weyl semimetal TaAs,” *Phys. Rev. X* **5**, 031013 (2015).
- [11] Alexey A Soluyanov, Dominik Gresch, Zhijun Wang, QuanSheng Wu, Matthias Troyer, Xi Dai, and B Andrei Bernevig, “Type-ii weyl semimetals,” *Nature* **527**, 495–498 (2015).
- [12] M. Zahid Hasan, Su-Yang Xu, Ilya Belopolski, and Shin-Ming Huang, “Discovery of weyl fermion semimetals and topological fermi arc states,” *Annual Review of Condensed Matter Physics* **8**, 289–309 (2017).
- [13] Hongming Weng, Chen Fang, Zhong Fang, B. Andrei Bernevig, and Xi Dai, “Weyl semimetal phase in noncentrosymmetric transition-metal monophosphides,” *Phys. Rev. X* **5**, 011029 (2015).
- [14] Nan Xu, HM Weng, BQ Lv, Christian E Matt, Jihwey Park, Federico Bisti, Vladimir N Strocov, Dariusz Gawryluk, Ekaterina Pomjakushina, Kazimierz Conder, *et al.*, “Observation of weyl nodes and fermi arcs in tantalum phosphide,” *Nature communications* **7**, 11006 (2016).
- [15] Ilya Belopolski, Su-Yang Xu, Daniel S. Sanchez, Guoqing Chang, Cheng Guo, Madhab Neupane, Hao Zheng, Chi-Cheng Lee, Shin-Ming Huang, Guang Bian, Nasser Alidoust, Tay-Rong Chang, BaoKai Wang, Xiao Zhang, Arun Bansil, Horng-Tay Jeng, Hsin Lin, Shuang Jia, and M. Zahid Hasan, “Criteria for directly detecting topological fermi arcs in weyl semimetals,” *Phys. Rev. Lett.* **116**, 066802 (2016).
- [16] Su-Yang Xu, Ilya Belopolski, Daniel S. Sanchez, Chenglong Zhang, Guoqing Chang, Cheng Guo, Guang Bian, Zhujun Yuan, Hong Lu, Tay-Rong Chang, Pavel P. Shibayev, Mykhailo L. Prokopovych, Nasser Alidoust, Hao Zheng, Chi-Cheng Lee, Shin-Ming Huang, Raman Sankar, Fangcheng Chou, Chuang-Han Hsu, Horng-Tay Jeng, Arun Bansil, Titus Neupert, Vladimir N. Strocov, Hsin Lin, Shuang Jia, and M. Zahid Hasan, “Experimental discovery of a topological weyl semimetal state in TaP,” *Science Advances* **1**, e1501092 (2015).
- [17] A. A. Zyuzin, Si Wu, and A. A. Burkov, “Weyl semimetal with broken time reversal and inversion symmetries,” *Phys. Rev. B* **85**, 165110 (2012).
- [18] A. A. Burkov, M. D. Hook, and Leon Balents, “Topological nodal semimetals,” *Phys. Rev. B* **84**, 235126 (2011).
- [19] Chen Fang, Hongming Weng, Xi Dai, and Zhong Fang, “Topological nodal line semimetals,” *Chinese Physics B* **25**, 117106 (2016).
- [20] Shuo-Ying Yang, Hao Yang, Elena Derunova, Stuart S. P. Parkin, Binghai Yan, and Mazhar N. Ali, “Symmetry demanded topological nodal-line materials,” *Advances in Physics: X* **3**, 1414631 (2018).
- [21] Guang Bian, Tay-Rong Chang, Hao Zheng, Saavanth Velury, Su-Yang Xu, Titus Neupert, Ching-Kai Chiu, Shin-Ming Huang, Daniel S. Sanchez, Ilya Belopolski, Nasser Alidoust, Peng-Jen Chen, Guoqing Chang, Arun Bansil, Horng-Tay Jeng, Hsin Lin, and M. Zahid Hasan, “Drumhead surface states and topological nodal-line fermions in TlTaSe₂,” *Phys. Rev. B* **93**, 121113 (2016).
- [22] Chen Fang, Yige Chen, Hae-Young Kee, and Liang Fu, “Topological nodal line semimetals with and without spin-orbital coupling,” *Phys. Rev. B* **92**, 081201 (2015).
- [23] Lilia S. Xie, Leslie M. Schoop, Elizabeth M. Seibel, Quinn D. Gibson, Weiwei Xie, and Robert J. Cava, “A new form of Ca₃P₂ with a ring of Dirac nodes,” *APL Materials* **3**, 083602 (2015).
- [24] Youngkuk Kim, Benjamin J. Wieder, C. L. Kane, and Andrew M. Rappe, “Dirac line nodes in inversion-symmetric crystals,” *Phys. Rev. Lett.* **115**, 036806 (2015).
- [25] Sandy Adhitha Ekahana, Shu-Chun Wu, Juan Jiang, Kenjiro Okawa, Dharmalingam Prabhakaran, Chan-Cuk Hwang, Sung-Kwan Mo, Takao Sasagawa, Claudia Felser, Binghai Yan, Zhongkai Liu, and Yulin Chen, “Observation of nodal line in non-symmorphic topological semimetal InBi,” *New Journal of Physics* **19**, 065007 (2017).
- [26] Qiunan Xu, Rui Yu, Zhong Fang, Xi Dai, and Hongming Weng, “Topological nodal line semimetals in the CaP₃

- family of materials,” *Phys. Rev. B* **95**, 045136 (2017).
- [27] D. Takane, Zhiwei Wang, S. Souma, K. Nakayama, C. X. Trang, T. Sato, T. Takahashi, and Yoichi Ando, “Dirac-node arc in the topological line-node semimetal HfSiS,” *Phys. Rev. B* **94**, 121108 (2016).
- [28] C. Chen, X. Xu, J. Jiang, S.-C. Wu, Y. P. Qi, L. X. Yang, M. X. Wang, Y. Sun, N. B. M. Schröter, H. F. Yang, L. M. Schoop, Y. Y. Lv, J. Zhou, Y. B. Chen, S. H. Yao, M. H. Lu, Y. F. Chen, C. Felser, B. H. Yan, Z. K. Liu, and Y. L. Chen, “Dirac line nodes and effect of spin-orbit coupling in the nonsymmorphic critical semimetals $m\text{SiS}$ ($m = \text{Hf, Zr}$),” *Phys. Rev. B* **95**, 125126 (2017).
- [29] Xiao-Bo Wang, Xiao-Ming Ma, Eve Emmanouilidou, Bing Shen, Chia-Hsiu Hsu, Chun-Sheng Zhou, Yi Zuo, Rong-Rong Song, Su-Yang Xu, Gan Wang, Li Huang, Ni Ni, and Chang Liu, “Topological surface electronic states in candidate nodal-line semimetal CaAgAs,” *Phys. Rev. B* **96**, 161112 (2017).
- [30] Po-Yao Chang, “Nodal-line semimetals and their variance,” *arXiv preprint arXiv:2507.02329* (2025), 10.48550/arXiv.2507.02329.
- [31] M. Z. Hasan and C. L. Kane, “Colloquium: Topological insulators,” *Rev. Mod. Phys.* **82**, 3045–3067 (2010).
- [32] M Zahid Hasan and Joel E Moore, “Three-dimensional topological insulators,” *Annu. Rev. Condens. Matter Phys.* **2**, 55–78 (2011).
- [33] Joel E Moore, “The birth of topological insulators,” *Nature* **464**, 194–198 (2010).
- [34] Xiao-Liang Qi and Shou-Cheng Zhang, “Topological insulators and superconductors,” *Rev. Mod. Phys.* **83**, 1057–1110 (2011).
- [35] Marcel Franz and Laurens Molenkamp, *Topological insulators*, Vol. 6 (Elsevier, 2013).
- [36] E. H. Hwang and S. Das Sarma, “Dielectric function, screening, and plasmons in two-dimensional graphene,” *Phys. Rev. B* **75**, 205418 (2007).
- [37] S. Das Sarma, E. H. Hwang, and Hongki Min, “Carrier screening, transport, and relaxation in three-dimensional dirac semimetals,” *Phys. Rev. B* **91**, 035201 (2015).
- [38] S. Das Sarma and E. H. Hwang, “Collective modes of the massless dirac plasma,” *Phys. Rev. Lett.* **102**, 206412 (2009).
- [39] Anmol Thakur, Rashi Sachdeva, and Amit Agarwal, “Dynamical polarizability, screening and plasmons in one, two and three dimensional massive dirac systems,” *Journal of Physics: Condensed Matter* **29**, 105701 (2017).
- [40] Chen-Huan Wu, “Dynamical polarization, plasmon model, and the friedel oscillation of the screened potential in doped dirac and weyl system,” *arXiv preprint arXiv:1809.00169* (2018), 10.48550/arXiv.1809.00169.
- [41] Seongjin Ahn, EH Hwang, and Hongki Min, “Collective modes in multi-weyl semimetals,” *Scientific reports* **6**, 34023 (2016).
- [42] Zoran Rukelj, Ivan Kupčić, and Danko Radić, “Density of states in the 3d system with semimetallic nodal-loop and insulating gapped phase,” *Symmetry* **16** (2024), 10.3390/sym16010038.
- [43] Hamid Rahimpour and Saeed H. Abedinpour, “Collective excitations and screening in two-dimensional tilted nodal-line semimetals,” *Phys. Rev. B* **109**, 045120 (2024).
- [44] Zhongbo Yan, Peng-Wei Huang, and Zhong Wang, “Collective modes in nodal line semimetals,” *Phys. Rev. B* **93**, 085138 (2016).
- [45] Shahin Barati and Saeed H. Abedinpour, “Optical conductivity of three and two dimensional topological nodal-line semimetals,” *Phys. Rev. B* **96**, 155150 (2017).
- [46] Chen Wang, Wen-Hui Xu, Chang-Yong Zhu, Jin-Na Chen, Yong-Long Zhou, Ming-Xun Deng, Hou-Jian Duan, and Rui-Qiang Wang, “Anomalous hall optical conductivity in tilted topological nodal-line semimetals,” *Phys. Rev. B* **103**, 165104 (2021).
- [47] R. Flores-Calderón, Leonardo Medel, and A. Martín-Ruiz, “Electrochemical transport in dirac nodal-line semimetals,” *Europhysics Letters* **143**, 16001 (2023).
- [48] Vivek Pandey, Dayana Joy, Dimitrie Culcer, and Pankaj Bhalla, “Longitudinal dc conductivity in dirac nodal line semimetals: Intrinsic and extrinsic contributions,” *Phys. Rev. B* **110**, 155108 (2024).
- [49] Vivek Pandey and Pankaj Bhalla, “Disorder induced dynamical interband response in dirac nodal line semimetals,” *physica status solidi (RRL) – Rapid Research Letters* **n/a**, 2500108 (2025).
- [50] Takahiro Chiba, Saburo Takahashi, and Gerrit E. W. Bauer, “Magnetic-proximity-induced magnetoresistance on topological insulators,” *Phys. Rev. B* **95**, 094428 (2017).
- [51] Piotr Kot, Jonathan Parnell, Sina Habibian, Carola Straßer, Pavel M. Ostrovsky, and Christian R. Ast, “Band dispersion of graphene with structural defects,” *Phys. Rev. B* **101**, 235116 (2020).
- [52] Qi Chen, Liang Du, and Gregory A. Fiete, “Floquet band structure of a semi-dirac system,” *Phys. Rev. B* **97**, 035422 (2018).
- [53] Bernardus Rendy and Eddwi Hesky Hasdeo, “Strain effects on band structure and Dirac nodal-line morphology of ZrSiSe,” *Journal of Applied Physics* **129**, 014306 (2021).
- [54] LuoJun Du, Tawfique Hasan, Andres Castellanos-Gomez, Gui-Bin Liu, Yuguai Yao, Chun Ning Lau, and Zhipei Sun, “Engineering symmetry breaking in 2d layered materials,” *Nature Reviews Physics* **3**, 193–206 (2021).
- [55] Y.-H. Chan, Ching-Kai Chiu, M. Y. Chou, and Andreas P. Schnyder, “ Ca_3P_2 and other topological semimetals with line nodes and drumhead surface states,” *Phys. Rev. B* **93**, 205132 (2016).
- [56] M. B. Schilling, L. M. Schoop, B. V. Lotsch, M. Dressel, and A. V. Pronin, “Flat optical conductivity in zrsis due to two-dimensional dirac bands,” *Phys. Rev. Lett.* **119**, 187401 (2017).
- [57] Vivek Pandey and Pankaj Bhalla, “Reshaping the anomalous hall response in tilted 3d system with disorder correction,” *New Journal of Physics* **27**, 073501 (2025).
- [58] Po-Yao Chang and Chuck-Hou Yee, “Weyl-link semimetals,” *Phys. Rev. B* **96**, 081114 (2017).